Quinn Y. J. Smithwick
Dept. of Aeronautics & Astronautics,
University of Washington,
Seattle, WA 98195;
Dept. of Mechanical Engr.,
University of Washington,
Seattle, WA 98195;
Human Interface Technology Lab,
University of Washington,
Seattle, WA 98195

Per G. Reinhall
Dept. of Mechanical Engr.,
University of Washington,
Seattle, WA 98195

Juris Vagners
Dept. of Aeronautics & Astronautics,
University of Washington,
Seattle, WA 98195

Eric J. Seibel
Dept. of Mechanical Engr.,
University of Washington,
Seattle, WA 98195;
Human Interface Technology Lab,
University of Washington,
Seattle, WA 98195

A Nonlinear State-Space Model of a Resonating Single Fiber Scanner for Tracking Control: Theory and Experiment

A nonlinear state-space dynamic model of a resonating single fiber scanner is developed to understand scan distortion—jump, whirl, amplitude dependent amplitude and phase shifts—and as the basis for controllers to remove those distortions. The non-planar nonlinear continuum dynamics of a resonating base excited cantilever are reduced to a set of state-space coupled Duffing equations with centripetal acceleration. Methods for experimentally determining the model parameters are developed. The analytic frequency responses for raster, spiral and propeller scans are derived, and match experimental frequency responses for all three scan patterns, for various amplitudes, and using the same model parameters. [DOI: 10.1115/1.1649974]

1 Introduction

At the University of Washington's Human Interface Technology Lab, small high-speed laser scanners with wide fields of view (fov) are being developed for various display and image acquisition applications. Among them is a resonating single fiber scanner, which has demonstrated a scan of 20 deg fov at 15.8 kHz. Its potential uses include a single fiber scanning endoscope—a flexible miniature endoscope that promises high resolution images in a package less than 3 mm in diameter [1].

The fiber scanner consists of a light-carrying single mode optical fiber attached to a quadrant piezoelectric tube at a point close to the fiber's distal end. The length of the fiber extending beyond the piezotube acts as base excited cantilever and is adjusted so the resonant frequency is the desired scan frequency. Opposite planar quadrants of the piezotube excite the fiber at the cantilever's resonant frequency. The low damping and resonant behavior of the fiber amplifies small tube displacements into large fiber tip displacements. Laser light coupled into the fiber emanates from the vibrating tip, producing a large field of view spot scan. See Fig. 1.

Once a spot scan is produced, the intensity of the light spot can be modulated for image display applications. For image acquisition applications, the intensity of the backscattered light from the spot scanned across a target can be collected. In both these applications, high quality scans are required. However, due to the dynamics of the resonating fiber, the scan may not follow an assumed reference pattern resulting in image distortion.

To understand and predict the fiber scanner's behavior we will derive a nonlinear dynamic model. This model will also serve as a basis for a nonlinear controller to force the scan to follow a defined reference regardless of the variability of the scanner's mechanical and dynamic parameters, thereby removing the distortion [2]. The parameters of resonant scanners may vary from scanner to scanner and in the same scanner due to manufacturing variability, environmental changes, and aging effects. Our goal is to derive a succinct model of the system dynamics describing the desired effects in the region of interest and verify it experimentally using typical scan patterns.

This model may be applicable to devices other than fiber scanners such as NSOM probes and various fiber optic sensors. According to Nayfeh [3], the motions of base excited cantilevers are of interest in connection with helicopter rotor blades, manipulator arms and spacecraft antennas. Additional control effort to damp out parametric excitation (whirl) of these structures has so far consisted of adding nonlinear damping terms proportional to the velocity cubed [4]. These controllers are somewhat *ad hoc*, being added and their effects investigated. With the development of equations describing the vibrations of base excited cantilevers in a form compatible with control theory, rigorous design and analysis of robust controller can be investigated.

1.1 Scan Patterns. Various scan patterns can be created by properly modulating the piezo's drive signal. A standard *z-y* raster scan uses the resonating fiber scanner for the fast horizontal scan and a galvo-mirror scanner for the slow vertical scan, as illustrated in Fig. 2*a*. For a standard VGA display, the fiber resonates with a constant amplitude sinewave of 15.7 kHz, and the galvo-mirror vibrates at 30 Hz. The disadvantage of using the galvo-mirror scanner is that it is large and heavy. The reflection off the mirror also results in a scanner geometry that is not axially symmetric, further increasing the size of the scanner. Removing the mirror scanner would result in significant weight, size, and power savings.

A piezotube with quartered electrodes is useful for creating two-dimensional resonant scan patterns with a single actuator because it provides both horizontal and vertical actuation. Because the movement of the piezotube is small, the fiber needs to resonate in both directions to produce a two-dimensional scan with a useable field-of-view. Since resonant amplification occurs only in a

Contributed by the Dynamic Systems, Measurement, and Control Division of THE AMERICAN SOCIETY OF MECHANICAL ENGINEERS for publication in the ASME JOURNAL OF DYNAMIC SYSTEMS, MEASUREMENT, AND CONTROL. Manuscript received by the ASME Dynamic Systems and Control Division August 21, 2003. Associate Editor: A. Alleyne

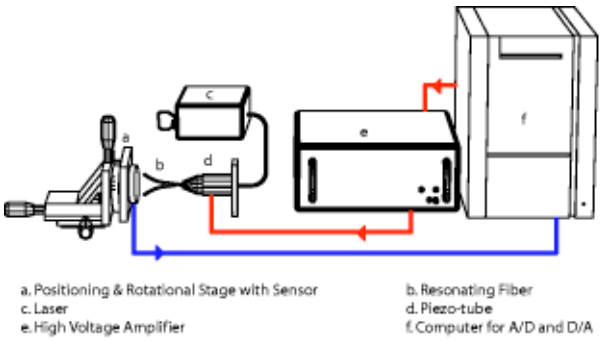

Fig. 1 Resonating Single Fiber Scanner and Experimental Setup

small range around each natural frequency, resonant scans are typically sinusoidal. Lissajous patterns result from *z*-*y* scans of two sinusoidal signals. If the two signals' frequency ratio can be expressed as a small integer or a rational number, a stable closed pattern is created. The frequency ratio for a 2-D resonant scanner is the ratio of the *z*-axis' natural frequency to the *y*-axis' natural frequency. The resonant single fiber scanner uses a standard circularly cylindrical optical fiber, so the *z* and *y* axes' natural frequencies are the same and 1:1 Lissajous patterns can be created. Depending on the amplitude and phase of the *z* and *y* scan, the 1:1 Lissajous pattern can take on a variety of shapes: skewed lines, rotated ellipses, and circles.

A circular scan results when the horizontal and vertical resonant vibrations are of the same frequency and equal amplitude but 90 deg out of phase. To create a space-filling spiral scan, the amplitudes of a circular scan are modulated in a triangle pattern while the phases are kept constant. Fig. 2*b*. In addition to a spiral scan, a ''propeller'' scan can be generated with a single piezotube, as seen in Fig. 2*c*. A 1:1 Lissajous pattern creates a 45 deg skewed line when the horizontal and vertical sinewaves are of the same frequency, equal amplitude and in-phase. To produce a space filling scan, this 45 deg linear ''radial'' scan is rotated in a continuous ''angular'' sweep by modulating the horizontal and vertical sinewaves' amplitudes such that the sum of their squares remains constant—one varies sinusoidally, the other varies cosinusoidally.

1.2 Image Distortion. In both image display and image acquisition applications, high quality scans are paramount. The dispersal or collection of the image data must be synchronized with the position of the scan. Typically, the data or pixel collection starts at the beginning of the scan and occurs sequentially at a constant rate commensurate with the scan frequencies. However, the scan cannot always be assumed to follow a known, regular, repeatable reference pattern, due to the piezotube and the resonant fiber dynamics, resulting in image distortion. Near resonance, the fiber can undergo large displacements taking it outside the region of linear dynamic behavior. Observed nonlinear dynamic effects include amplitude dependant phase shifts, nonlinear amplitude response, amplitude jumps, and whirl.

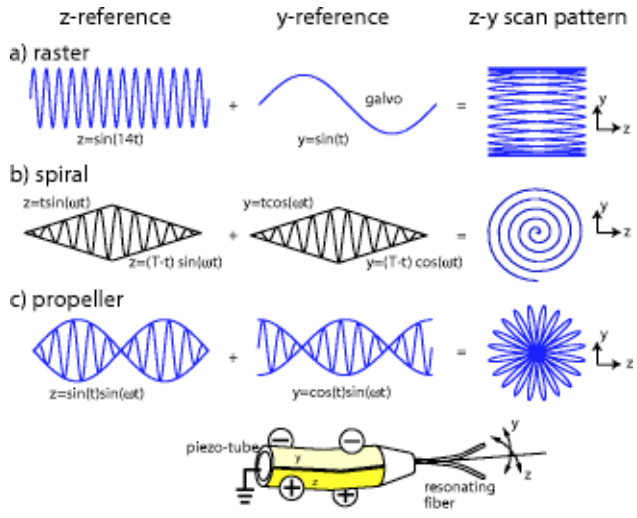

Fig. 2 Scan Patterns with *z* and *y* components

The amplitude dependant phase shifts and nonlinear amplitude response mainly affect the polar spiral and propeller scans since they both depend on amplitude modulation for creating a space-filling scan. The amplitude dependent phase shift manifests itself as warped radial lines in the images created with a spiral scan. In the propeller scan, the radial scan line will become elliptical because the *z* and *y* scans are of different amplitudes and therefore have different phase shifts. The elliptical radial scan results in blurred or incoherent images. The amplitude dependent phase shift does not regularly affect the raster scan since it consists of a constant amplitude sinewave. However, if the amplitude of the raster scan is changed, say to decrease the field-of-view to produce a zoomed scan [1], the amplitude dependant phase shift will cause a loss of synchronization with the data input/output resulting in a distorted image.

Likewise, the nonlinear amplitude response mainly affects the amplitude modulated polar scans. The inner radii will be nearly linearly spaced while the outer radii will be expanded due to the nonlinear amplitude response. This results in a ''fish-eye'' appearance in the images created with a spiral or propeller scan. Again, the raster scan does not suffer as greatly from this effect because of its constant amplitude scan. However, the zooming will not be linear with change in drive amplitude.

Amplitude jumps are sudden changes in fiber tip amplitudes with the same drive frequency and amplitude. At certain frequencies, there are two stable vibration amplitudes and small disturbances will cause the amplitude to change from one to the other. In medical imaging or display applications this sudden and unanticipated change in field of view can be catastrophic.

Whirl is an undriven out-of-plane response. For a raster scan, although the fiber is being only excited horizontally, there may be a vertical response in addition to the horizontal vibration. This vibration causes the scan to take on a skewed linear, rotated ellipse, or a circular shape instead of the ideally horizontal linear pattern. Depending on the severity of the whirl, the resulting images are distorted, blurred, or incoherent. The effects of whirl are not as apparent in the spiral or propeller scan, possibly because they are being driven in both the *z* and *y* planes simultaneously. Whirl may contribute to the elliptical radial scan line in the propeller scan, in addition to the amplitude dependant phase shift mentioned previously.

2 Dynamic Model

To understand the behavior of the scanner, we need a nonlinear dynamic model. The model will also serve as a basis for the design of a nonlinear controller to force the scan to follow a defined reference regardless of the dynamics thereby removing the distortion. Our goal is to derive a succinct model of the system dynamics that describes the desired effects in the region of interest; i.e., find the minimum model description that contains the amplitude dependence of phase and amplitude, the jump phenomena and whirl.

The main parts of the fiber scanner are the optical fiber, which carries the light and whose vibration scans the light; and the piezotube, which excites the fiber. The dominant system dynamics are expected to be from the large amplitude resonant vibrations of

the fiber. We consider the fiber as a base excited cantilever undergoing transverse vibrations and investigate the dynamics near the resonant frequency.

2.1 Base Excited Cantilever Continuum Model. Haight and King [5] used a set of two-dimensional cross-coupled partial integro-differential equations for a transverse base excited cantilever that included longitudinal and nonlinear inertial effects, but ignored nonlinear curvature for their analysis. Crespo da Silva [6] found that the nonlinear curvature can not be ignored and derived a more complete set of torsional-flexural-flexural partial integro-differential equations for a transverse base excited cantilever that retained longitudinal inertia, nonlinear inertia and nonlinear curvature effects. Pai and Nayfeh [3] extended Crespo da Silva's derivation to include gravitational effects and motion in a fixed frame reference rather than a base frame reference. The equations given by Pai and Nayfeh are

$$\ddot{v}+c\dot{v}+\beta_y v''''=(1-\beta_y)\left[w''\int_1^s v''w''ds-v'''\int_0^s w''v'ds\right]'-[(1-\beta_y)^2/\beta_y]\left(w''\int_0^s\int_1^s v''w''dsds\right)''-\beta_y[v'(v'v''+w'w'')']'-\frac{1}{2}\left\{v'\int_1^s\left[\int_0^s(v'^2+w'^2)ds\right]ds\right\}'+[v''(s-1)+v'](L^3/D_\eta)mg \tag{1a}$$

$$\ddot{w}+c\dot{w}+\beta_y w''''=-(1-\beta_y)\left[v''\int_1^s v''w''ds-v'''\int_0^s w''v'ds\right]'-[(1-\beta_y)^2/\beta_y]\left(v''\int_0^s\int_1^s v''w''dsds\right)''-[w'(w'w''+v'v'')']'-\frac{1}{2}\left\{w'\int_1^s\left[\int_0^s(v'^2+w'^2)ds\right]ds\right\}'+[w''(s-1)+w'](L^3/D_\eta)mg+F\Omega^2\cos\Omega t+cF\Omega\sin\Omega t \tag{1b}$$

Note: dots are temporal differentiation, primes are spatial differentiation. See Fig. 3.

For a symmetrical homogeneous beam like the fiber, the ratio of the principal stiffnesses are approximately the same, $\beta_y=1+\varepsilon^2\delta\approx 1$. The $\varepsilon^2\delta$ term allows slight asymmetry of the fiber, but the β_y-1 terms will be of higher order than the derivation's third order expansion of the nonlinearities and therefore the bending-torsional cross coupling disappears [3]. With $\beta_y=1+\varepsilon^2\delta$ and ignoring gravitational effects, Eqs. (1*a*,*b*) become

$$\ddot{v}+c\dot{v}+\beta_y v''''=-\{v'(v'v''+w'w'')'\}'-\frac{1}{2}\left\{v'\int_1^s\left[\int_0^s(v'^2+w'^2)ds\right]ds\right\}' \tag{2a}$$

$$\ddot{w}+c\dot{w}+w''''=-\{w'(v'v''+w'w'')'\}'-\frac{1}{2}\left\{w'\int_1^s\left[\int_0^s(v'^2+w'^w)ds\right]ds\right\}'+F\Omega^2\cos\Omega t+cF\Omega\sin\Omega t \tag{2b}$$

The first term on the right hand side of Eq. 2*a* or Eq. 2*b* is due to nonlinear curvature, while the second term on the right hand side is due to nonlinear inertia. Pai and Nayfeh use a fixed frame of reference, which leads to excitation of the form $cF\Omega\sin\Omega t+F\Omega^2\cos\Omega t$. This is equivalent to the general $c\dot{u}+\Omega^2 u$ excitation term of a base excited structure in a fixed frame of reference with base motion $u=F\cos\Omega t$. We replace the sinusoidal base motion with general excitation and also include the possibility of excitation in both axes, u_z and u_y. For small displacements, light damping and $\Omega^2\approx 1$, we get

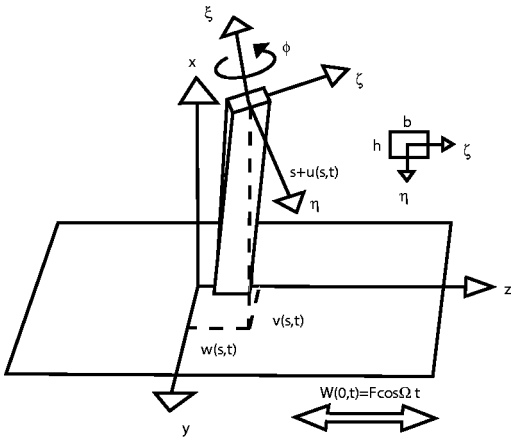

Fig. 3 Coordinate systems for a base excited cantilever *x*, *y* and *z* are the inertial coordinates; *t* is the time; *s* is the undeformed arc length (material coordinate); ξ, η, ζ are the principle axes of the beam's cross section at position *s*; D_ξ, D_η, D_ζ are the principle stiffnesses; $\beta_y=D_\zeta D_\eta$ and $\beta_y=D_\xi/D_\eta$; $u(s,t)$, $v(s,t)$, and $w(s,t)$ are the components of the displacement of the centroid at an arbitrary location *s* along the inertial axes *x*, *y* and *z* respectively, and *g* denotes the acceleration due to gravity. *F* and Ω are the constant amplitude and frequency of the base motion. All variables are nondimensionalized using the constrained length of the beam *L* and the characteristic times $L^2\sqrt{m/D_\eta}$ where *m* is the mass per unit length. The following assumptions are made: (*a*) the cross-section dimensions *b* and *h* and material properties are uniform, (*b*) the distributed torsional moments of inertia of the beam are negligible, (*c*) the dissipation of energy due to internal friction, resistance and relative motion between the beam and its support system can be modeled by a viscous damper having the coefficient *c*. [3]

$$\ddot{v}+c\dot{v}+\beta_y v''''=-\{v'(v'v''+w'w'')'\}'-\frac{1}{2}\left\{v'\int_1^s\left[\int_0^s(v'^2+w'^2)ds\right]ds\right\}'+u_y \tag{3a}$$

$$\ddot{w}+c\dot{w}+w''''=-\{w'(v'v''+w'w'')'\}'-\frac{1}{2}\left\{w'\int_1^s\left[\int_0^s(v'^2+w'^2)ds\right]ds\right\}'+u_z \tag{3b}$$

2.2 Discrete Modal Nonlinear Ordinary Differential Equations. The partial integro-differential equations (3*a*,*b*) can be reduced to ordinary differential equations by an application of Galerkin's method with the assumption of linear mode shapes, $\Phi(x)$, for cantilevers, and allowing for nonlinear temporal responses p and q in the z and y axes respectively.

$$v(x,t)=\Phi(x)q(t),\quad w(x,t)=\Phi(x)p(t) \tag{4a}$$

$$\Phi(x)=\sin\beta x-\sinh\beta x+a(\cos\beta x-\cosh\beta x) \tag{4b}$$

where a and β depend on mode number n

Substitution of Eqs. 4*a*,b into Eqs. 3*a*,b yields equations for the temporal responses.

$$\ddot{p}+\varepsilon c\dot{p}+p=\varepsilon k_1(-p^3-pq^2)-\varepsilon k_2 p(\dot{p}^2+p\ddot{p}+\dot{q}^2+q\ddot{q})+\varepsilon Cu_z \tag{5a}$$

$$\ddot{q}+\varepsilon c\dot{q}+\omega_y^2 q=\varepsilon k_1(-q^3-p^2q)-\varepsilon k_2 q(\dot{p}^2+p\ddot{p}+\dot{q}^2+q\ddot{q})+\varepsilon Cu_y \tag{5b}$$

where $k_1=\int_0^1\Phi_m[\Phi_n'(\Phi_n'\Phi_n'')']'ds$ is a constant related to the nonlinear curvature contributions, $k_2=\int_0^1\Phi_m[\Phi_n'\int_1^s\int_0^s\Phi_n'^2 dsds]'ds$ is a constant related to the nonlinear inertia contributions, and $C=\int_0^1\Phi_m ds$.

We have introduced a book keeping parameter ε to group terms of similar importance. From experimental experience, we know the system is weakly nonlinear, lightly damped and subjected to weak excitation.

It is necessary in modern control theory to describe the dynamics in terms of its state variables $(p,\dot{p},q,\dot{q})$. Solving for $\ddot{p}$ and $\ddot{q}$ in Eqs. 5, letting $\omega_y^2=1+\varepsilon\delta$, then expanding the solutions using Taylor series in terms of ε and retaining only the terms of order ε, the differential equations reduce to

$$\ddot{p}+\varepsilon c\dot{p}+p=-\varepsilon k_3 p(p^2+q^2)-\varepsilon k_2 p(\dot{p}^2+\dot{q}^2)+\varepsilon Cu_x \tag{6a}$$

$$\ddot{q}+\varepsilon c\dot{q}+\omega_y^2 q=-\varepsilon k_3 q(q^2+p^2)-\varepsilon k_2 q(\dot{p}^2+\dot{q}^2)+\varepsilon Cu_y \tag{6b}$$

$$\text{where}\quad k_3=(k_1-k_2) \tag{6c}$$

This is a set of cross-coupled Duffing equations with centripetal acceleration. The coefficient on the cubic spring term $-\varepsilon k_3 p(p^2+q^2), k_3=(k_1-k_2)$ is a combination of the nonlinear curvature, k_1, and nonlinear inertia, k_2. The nonlinear curvature adds a hardening spring effect, while the nonlinear inertia adds a softening spring effect. This is in agreement with Crespo da Silva and Glynn's [6] observations. The cross-coupled centripetal acceleration term $-\varepsilon k_2 p(\dot{p}^2+\dot{q}^2)$ is due to longitudinal and nonlinear inertia effects.

The terms of order ε^2 contain nonlinearities of order five; i.e. $qp^4, qp^2\dot{p}^2$, etc. Crespo da Silva and Glynn's [6] partial integro-differential equations were expanded such that perturbation analysis would only retain nonlinearities up to order three; i.e. $q^3, qp^2, q\dot{p}^2$, etc. Therefore, the order five nonlinearities are of higher order than the original derivation accounted for and can therefore be ignored. The order ε^2 terms also contain nonlinear damping terms $\varepsilon^2 k_2 cp(p\dot{p}+q\dot{q}), \varepsilon^2 k_2 cq(p\dot{p}+q\dot{q})$ and nonlinear forcing terms $\varepsilon^2 k_2 Cp(pu_x+qu_y), \varepsilon^2 k_2 Cq(pu_x+qu_y)$. Damping was included in the original equations *ad hoc* and assumed to be linear, so we should feel no obligation to retain these nonlinear terms. Instead we can add the viscous and aerodynamic damping directly to the state space equations. As for the nonlinear forcing terms, we can consider them higher order terms and ignore them.

2.3 Damping Models. Nonlinear effects and damping affect the dynamic response of the fiber mainly in the frequency regions of large deflections near resonance. We must therefore carefully consider how damping limits the deflection of the fiber. In the original partial integro-differential equations (Eqs. 1*a*,b), viscous damping was added somewhat *ad hoc*. Viscous damping is a commonly used model for damping because it is linear, and for harmonic motion, there is an equivalent viscous damping to other forms of damping. We will examine the forms of internal damping and aerodynamic drag and determine whether a viscous approximation is appropriate. We examine two models for internal damping: imperfect elasticity and solid damping.

2.3.1 Imperfect Elasticity. The imperfect elasticity model, a type of viscoelastic damping, is the form most commonly used in linear analysis of fiberoptic probes for near-field scanning optical microscopy (NSOM) [7]. NSOM probes use a resonating optical fiber cantilever and are similar to the fiber scanner except large displacements do not occur. The stress acting on the body is assumed to be proportional to the strain and the rate of strain. $\sigma=E\varepsilon+\gamma\dot{\varepsilon}=E(\varepsilon+\alpha\dot{\varepsilon})$. From an analysis of the linear continuum mechanics with this damping model, the spatial mode shape solution results in a complex stiffness term and the temporal dynamics solution contains a linear viscous term. Although this model is commonly used in NSOM probe linear dynamic analysis and has given good experimental results [1,7,8], the imperfect elasticity assumption is actually not appropriate. Experiments performed by Kimball and Lovell [9] indicate that when glass is subjected to cyclic stress, the internal friction is independent of the rate of strain and is dependent on the amplitude over a considerable frequency range.

2.3.2 Solid Damping. A model of the drag force, F_d, for structural damping that incorporates the behavior discussed by Kimball and Lovell is the solid damping model [10,11], a type of hysteretic damping.

$$F_d=-\frac{\beta}{2}\,\mathrm{sgn}(\dot{p})|p| \tag{7a}$$

with the equivalent viscous damping coefficient

$$c_{eq}=\beta/\pi\omega \tag{7b}$$

The equivalent damping coefficient, c_{eq}, is inversely proportional to the vibration frequency, ω. In this research, the frequency range of interest is near the fiber's resonance, which is very narrow for light damping. The equivalent damping coefficient should be nearly constant in the region of interest. Therefore, viscous damping with a constant coefficient can be considered a reasonable approximation for solid damping in the fiber.

2.3.3 Aerodamping. The fiber has a circular cross-section and is vibrating in air (for the experiments reported here). For moderate speeds (high Reynolds's number), pressure forces dominate over frictional viscous air drag. The aerodynamic drag force (aerodamping) [10,11], F_d, can be approximated by

$$F_d=-\alpha\,\mathrm{sgn}(\dot{p})\dot{p}^2=-\alpha|\dot{p}|\dot{p} \tag{8a}$$

with equivalent viscous damping coefficient, c_{eq}, of

$$c_{eq}=\frac{8}{3\pi}\alpha\omega P, \tag{8b}$$

where P is the amplitude of the sinusoidal response p of frequency ω.

We see that the equivalent viscous damping increases with frequency and is proportional to the amplitude of the response. Most of the effects of the aerodynamic drag occur therefore at the sharp resonant peak with significantly less effect elsewhere. Also, because the spiral and propeller scan patterns are amplitude modulated, the effect of nonlinear aerodynamic drag can become important. Therefore, an equivalent viscous damping term is inappropriate in this case and we need to add an additional damping component into the dynamic equations to explicitly include aerodynamic damping.

2.4 Piezotube Actuator Dynamics. The amplitude of the base excitation is not a directly controlled parameter. The voltage applied to the piezotube is the input to the system. The movement of the piezotube's free end provides the base excitation for the fiber. Since we control the command voltages, not the base movement directly, we must be concerned with the piezotube dynamics.

Ideally, a piezotube can be modeled as a linear second-order system—a bending tube [12,13]. The bending is extremely small and therefore the end motion can be approximated by a translation. The piezotube is massive and stiff enough that the motion of the fiber does not affect the motion of the tube. If we drive the piezotube with a sinusoidal voltage of a frequency well below its first resonant frequency, we expect the piezotube's end motion to be sinusoidal with an amplitude linearly related to the drive voltage amplitude and in phase with the drive sinusoid. Preliminary experimental evidence showed that in the frequency range of in-

terest, the piezotube output is sinusoidal, nearly in-phase with the input, and with a constant input/output amplitude ratio. Thus, we consider the base excitation amplitude, u, to be linearly related to the input voltage, v.

$$Cu_i = Kv_i \quad (i=z,y) \tag{9}$$

Although a piezotube ideally acts as a linear second-order system, there are two main nonlinearities which affect piezoelectric materials—creep (or drift) and hysteresis. Aging is also a concern and that is one of the goals of adding a controller to the system. Since we are vibrating the tube at high frequencies without a DC component, creep is not a concern. Hysteresis acts as a delay on the system, introducing an undesirable phase shift between the input and output, and can distort the output. A phase shift adversely affects the image quality and would reduce the stability of any controller. Since the preliminary experiments showed the piezotube output is sinusoidal, nearly in-phase with the input, and with almost a constant input/output amplitude ratio, the hysteresis curve must be very narrow. If a narrow hysteresis curve is approximated as a straight line, then the input is proportional to the output and the hysteresis nonlinearity can be ignored.

2.5 Sensor Dynamics. To complete the loop for feedback control of the fiber scanner or to make experimental observations of the fiber's tip displacement, a position sensor is used. The light emanating from the fiber tip is projected onto the position sensor—a duolateral position sensing photodiode—and a voltage related to its position is produced. The light emanating from the fiber follows a straight line in the direction of the fiber's tip angle to the sensor. If the fiber's tip is extremely close to the position sensing photodiode, the difference between the tip position and the light spot on the photodiode will be small. If the position sensor's voltage is linearly proportional the position of the light spot on its surface, and its response is fast enough, the position's sensor's voltages, $\tilde{p}$ and $\tilde{q}$, are linearly proportional to the fiber's tip positions, p and q.

$$\tilde{p} \cong sp, \quad \tilde{q} \cong sq \tag{10}$$

2.6 Nonlinear State-Space System Dynamics. With the nonlinear fiber dynamics—the coupled Duffing equation with centripetal acceleration, aerodamping, equivalent viscous damping of solid damping, proportional actuation in z and y-axes, and proportional sensors—the equations of motion for the system become

$$\ddot{p} + \varepsilon c\dot{p} + \varepsilon\alpha|\dot{p}|\dot{p} + p = -\varepsilon k_3 p(p^2+q^2) - \varepsilon k_2 p(\dot{p}^2+\dot{q}^2) + \varepsilon K v_z \tag{11a}$$

$$\ddot{q} + \varepsilon c\dot{q} + \varepsilon\alpha|\dot{q}|\dot{q} + \omega_y^2 q = -\varepsilon k_3 q(p^2+q^2) - \varepsilon k_2 q(\dot{p}^2+\dot{q}^2) + \varepsilon K v_y \tag{11b}$$

$$\tilde{p} = sp, \tag{11c}$$

$$\tilde{q} = sq \tag{11d}$$

The equations are normalized with respect to the resonant frequency in the z direction $(p), \omega_z$. Note that, the bookkeeping coefficient ε has been retained.

The parameters $\omega_z, \omega_y, \varepsilon c, \varepsilon\alpha, \varepsilon k_3, \varepsilon k_2, \varepsilon K$ can be determined by comparing the theoretical frequency response with the frequency response obtained experimentally at a given sinusoidal forcing amplitude, $v_z = F_z \cos \Omega t$.

3 Frequency Response

To determine the frequency response of the system, we follow the analysis by Ho, Scott, and Eisley [14] for the large amplitude whirling motions of a simply supported beam including the response curves and the stability of motion. The dynamic equations they derived for the simply supported beam are cross-coupled Duffing equations (no centripetal acceleration). They used harmonic balance to determine the response curves for the undamped case with actuation in only one-plane. We will extend their results to the damped Duffing equation with centripetal acceleration with actuation appropriate for raster, spiral and propeller scans.

We rewrite the system Equations 11*a–d* as

$$\ddot{p} + \bar{\varepsilon} b\dot{p} + \overline{\varepsilon\alpha}|\dot{p}|\dot{p} + p = -\bar{\varepsilon} p(p^2+q^2) - \varepsilon_2 p(\dot{p}^2+\dot{q}^2) + \bar{\varepsilon}\bar{C} v_z \tag{12a}$$

$$\ddot{q} + \bar{\varepsilon} b\dot{q} + \overline{\varepsilon\alpha}|\dot{q}|\dot{q} + \omega_y^2 q = -\bar{\varepsilon} q(p^2+q^2) - \varepsilon_2 q(\dot{p}^2+\dot{q}^2) + \bar{\varepsilon}\bar{C} v_y \tag{12b}$$

where, $\bar{\varepsilon} = \varepsilon k_3$, $b = c/k_3$, $\bar{\alpha} = \alpha/k_3$, $\bar{C} = K/k_3$, $\varepsilon_2 = \varepsilon k_2$. The bar notation will be hereafter dropped.

In these equations, p and q can be considered the fiber tip's position in the z and y direction respectively, and the coefficients are εb, equivalent viscous damping; $\varepsilon\alpha$, aerodynamic drag; εC, forcing; ε, nonlinear spring; and ε_2, centripetal acceleration coefficients.

3.1 General Sinusoidal Frequency Response. We will derive the frequency response of the system for general sinusoidal excitation in both directions, then make appropriate reductions for each scan pattern. Although there is amplitude modulation in the spiral and propeller scan's forcing functions and responses, it occurs on a slower time scale compared with the faster time scale sinusoidal vibrations. Therefore, we use the Poincare-Lindstedt method to determine the steady-state frequency response of the fiber to harmonic inputs with constant amplitudes in both planes, from Eqs. 12*a* and 12*b*.

We use the following assumed solutions $p = A_x \cos(\Omega t + \phi_2)$, $q = A_y \cos(\Omega t + \phi_3 + \phi_1)$ with driving forces of $v_z = F_z \cos(\Omega t)$, $v_y = F_y \cos(\Omega t + \phi_1)$ where ϕ_1 is the phase difference between the driving forces v_z and v_y, ϕ_2 is the phase difference between v_z and p; ϕ_3 is the phase difference between v_y and q; and A_z, A_y are the response amplitudes. Let $\phi_4 = \phi_3 + \phi_1$, the phase difference between v_z and q. Substitution of the assumed solutions and driving forces, Fourier expansion of the $|\sin(\Omega t)|$ coefficient, and equating the secular terms to zero leads to a set of four implicit equations in A_z, A_y, ϕ_1, ϕ_2:

$$-\frac{1}{4}A_z A_y^2(-\varepsilon + \Omega^2\varepsilon_2)\sin(2\phi_2 - 2\phi_4) - \varepsilon b A_z\Omega - \frac{8}{3\pi}\varepsilon a A_z^2\Omega^2 = \varepsilon C F_z \sin\phi_2 \tag{13a}$$

$$\frac{1}{4}(\varepsilon - \varepsilon_2\Omega^2)A_z A_y^2\cos(2\phi_2 - 2\phi_4) + \frac{1}{2}(\varepsilon + \varepsilon_2\Omega^2)A_z A_y^2 + \frac{1}{4}A_z^3(3\varepsilon + \varepsilon_2\Omega^2) + (1-\Omega^2)A_z = \varepsilon C F_z \cos\phi_2 \tag{13b}$$

$$\frac{1}{4}A_z^2 A_y(-\varepsilon + \Omega^2\varepsilon_2)\sin(2\phi_2 - 2\phi_4) - \varepsilon b A_y\Omega - \frac{8}{3\pi}\varepsilon a A_y^2\Omega^2 = \varepsilon C F_y \sin\phi_3 \tag{13c}$$

$$\frac{1}{4}(\varepsilon - \varepsilon_2\Omega^2)A_z^2 A_y\cos(2\phi_2 - 2\phi_4) + \frac{1}{2}(\varepsilon + \varepsilon_2\Omega^2)A_z^2 A_y + \frac{1}{4}A_y^3(3\varepsilon + \varepsilon_2\Omega^2) + (\omega_y^2 - \Omega^2)A_y = \varepsilon C F_y \cos\phi_3 \tag{13d}$$

3.1.1 Raster Scan With Centripetal Acceleration. These equations can be used to find the frequency responses of the cross-coupled Duffing with centripetal acceleration for a raster scan. Setting $F_y = 0$, Eqs. 13*a–d* can be further manipulated to yield

$$\left[\varepsilon b\Omega(A_z^2+A_y^2)+\frac{8}{3\pi}\varepsilon\alpha\Omega^2(A_z^3+A_y^3)\right]^2+\left\{\frac{1}{4}[(\Omega^2\varepsilon_2+3\varepsilon)(A_z^4 - A_y^4)-4(\Omega^2-1)A_z^2+4(\Omega^2-\omega_y^2)A_y^2]\right\}^2=(\varepsilon FA_z)^2 \quad (14a)$$

$$\left\langle\left(\varepsilon b\Omega+\frac{8}{3\pi}\varepsilon\alpha\Omega^2A_y\right)^2+\left\{\frac{1}{4}[2(\varepsilon+\varepsilon_2\Omega^2)A_z^2+(3\varepsilon+\varepsilon_2\Omega^2)A_y^2 + 4(\omega_y^2-\Omega^2)]\right\}^2-\left[\frac{1}{4}(\varepsilon-\varepsilon_2\Omega^2)A_z^2\right]^2\right\rangle A_y^2=0 \quad (14b)$$

The equations for the raster scan's frequency response are a set of implicit equations in the amplitudes of the response A_z, A_y; and the amplitude and frequency of base excitation, F, Ω in the unknown parameters b, ε, ε_2 and C. See Eqs. 12*a* and 12*b* for parameter definitions. Note the trivial $A_y=0$ solution.

When $A_y=0$, the secular Eqs. 13*a*–13*d* can be manipulated to yield the planar amplitude frequency response

$$\left[\varepsilon b\Omega+\frac{8}{3\pi}\varepsilon\alpha\Omega^2A_z\right]^2+\left\{\frac{1}{4}(\Omega^2\varepsilon_2+3\varepsilon)A_z^2+(1-\Omega^2)\right\}^2 =(\varepsilon F/A_z) \quad (15a)$$

and the planar phase frequency response

$$\tan\phi_2=-\frac{\left(\varepsilon b\Omega+\frac{8}{3\pi}\varepsilon aA_z\Omega^2\right)}{\left[\frac{1}{4}A_z^2(3\varepsilon+\varepsilon_2\Omega^2)+(1-\Omega^2)\right]^2} \quad (15b)$$

3.1.2 Spiral Scans. For the spiral scan, the forcing functions are 90 deg apart. $\phi_1=-\pi/2$, $\phi_4=\phi_3-\pi/2$ ($v_z=F\cos\Omega t, v_y=F\sin\Omega t$). For simplicity, let $\omega_y=1$. Due to symmetry, let $A=A_z=A_y$. Also, the phase of the *z*-direction and the *y*-direction in relation to their plane's actuation should be the same, $\phi_3=\phi_2$. Note that $A_z=A_y, \phi_3=\phi_2$ may not be the only solution in this case. Eqs. 13*a*–13*d* become

$$-\varepsilon bA\Omega-\frac{8}{3\pi}\varepsilon aA^2\Omega^2=\varepsilon CF\sin\phi_2 \quad (16a)$$

$$(\varepsilon+\varepsilon_2\Omega^2)A^3+(1-\Omega^2)A=\varepsilon CF\cos\phi_2 \quad (16b)$$

which can be combined to

$$\left(\varepsilon b\Omega+\frac{8}{3\pi}\varepsilon\alpha\Omega^2A\right)^2+[(\varepsilon+\varepsilon_2\Omega^2)A^2+1-\Omega^2]^2-(\varepsilon CF/A)^2=0 \quad (17)$$

3.1.3 Propeller Scans. For the propeller scan the forcing functions are in phase. $\phi_1=0$, $\phi_4=\phi_3$ ($v_z=F\cos\Omega t, v_y=F\cos\Omega t$)

For simplicity, let $\omega_y=1$. Due to symmetry, let $A=A_z=A_y$. Also, the phase of the z-direction and the y-direction in relation to their plane's actuation should be the same, $\phi_3=\phi_2$. Note that $A_z=A_y, \phi_3=\phi_2$ may not be the only solution in this case. Eqs. 13*a*–*d* become

$$-\varepsilon bA\Omega-\frac{8}{3\pi}\varepsilon aA^2\Omega^2=\varepsilon CF\sin\phi_2 \quad (18a)$$

$$\left(\frac{3}{2}\varepsilon+\frac{1}{2}\varepsilon_2\Omega^2\right)A^3+(1-\Omega^2)A=\varepsilon CF\cos\phi_2 \quad (18b)$$

which can be combined to

$$\left(\varepsilon b\Omega+\frac{8}{3\pi}\varepsilon\alpha\Omega^2A\right)^2+\left[\left(\frac{3}{2}\varepsilon+\frac{1}{2}\varepsilon_2\Omega^2\right)A^2+1-\Omega^2\right]^2 -(\varepsilon CF/A)^2=0 \quad (19)$$

3.3 Stability of the Raster Scan's Out-of-Plane Response. Although linear theory predicts that the amplitude of the raster scan's undriven out-of-plane component is zero, $A_y=0$, using perturbation analysis we will see that the cross-coupling in the dynamics leads to an instability in the cross-plane axis for base excitations only in the in-plane direction.

The undamped Duffing equations with centripetal acceleration (Eqs. 12*a*,b, $\alpha=b=0, \varepsilon Cv_z=F\cos(\Omega t+\phi)$) are

$$\ddot{p}+p=-\varepsilon p(p^2+q^2)-\varepsilon p(\dot{p}^2+\dot{q}^2)+F\cos(\Omega t+\phi) \quad (20a)$$

$$\ddot{q}+q=-\varepsilon q(p^2+q^2)-\varepsilon q(\dot{p}^2+\dot{q}^2) \quad (20b)$$

Let's examine perturbations to the in-plane response by setting $q=0$ and $\dot{q}=0$.

$$\ddot{p}+p+\varepsilon p^3+\varepsilon_2 p\dot{p}^2=F\cos(\Omega t+\phi) \quad (21)$$

For weak excitation, the solution to Eq. 21 can be approximated by $p=P\cos\Omega t$. To investigate the stability of this solution let $q=q_0+\eta$, with $q_0=0$ and $\eta\ll1$. Substituting $q=\eta$ into Eq. 20*b* yields

$$\ddot{\eta}+(1+\varepsilon p^2+\varepsilon_2 p\dot{p}^2)\eta=0 \quad (22)$$

Substituting in the solution $p=P\cos\Omega t$ into the perturbed equation of motion, Eq. 22, expanding the cosine squared term, and rescaling the time $\tau=2\Omega t$ results in

$$\eta''+(\alpha+\beta\cos t)\eta=0 \quad (23a)$$

$$\alpha=\frac{1}{4\Omega^2}\left[1+\frac{1}{2}P^2(\varepsilon+\varepsilon_2\Omega^2)\right]. \quad (23b)$$

$$\beta=\frac{1}{4\Omega^2}\left[\frac{1}{2}P^2(\varepsilon-\varepsilon_2\Omega^2)\right] \quad (23c)$$

where primes are derivatives with respect to the scaled time τ.

This is a form of Mathieu's equation. It is well known that for given values of α and β, there are unbounded solutions, bounded solutions that are not periodic, and periodic solutions of period 2π or 4π [15]. We are interested in periodic solutions of period 4π, which corresponds to circular whirl.

The Mathieu equation has periodic solutions of period 4π when

$$\alpha=\frac{1}{4}\pm\frac{1}{2}\beta \quad \text{for small} \quad \beta \quad (24)$$

Substituting Eqs. 23*b*, 23*c* into Eq. 24, expanding the solution of Ω^2 in terms of ε and ε_2, and keeping only the first order terms in ε and ε_2 yields,

$$\Omega^2=1+\frac{1}{4}(\varepsilon+3\varepsilon_2)P^2$$

or

$$\Omega^2=1+\frac{1}{4}(3\varepsilon+\varepsilon_2)P^2 \quad (25)$$

So, we see near resonance $\Omega\cong1$, a periodic solution of period 4π is allowed. Since the parametric excitation is twice the frequency of the driving force, a solution to Mathieu's equation with a period of 4π would correspond to a perturbed out-of-plane response that is equal to the frequency of the in-plane response. Therefore, a response will trace out a 1:1 Lissajous pattern, such as a circle, ellipse, or skewed line, in the *z*-*y* plane. The cross coupling of the axes results in an instability when the driving frequency is near resonance leading to stable motion known as whirling. For the damped Mathieu's equation, the results are similar except damping prevents the formation of whirl for small driving amplitudes.

Following the above procedure for solutions of period 2π, when $\alpha=-1/2\beta^2$, and ignoring third or higher order terms in ε

and ε_2, leads to the imaginary frequencies $\Omega^2=-(1/32\varepsilon^2P^4)$ or $\Omega^2\cong-(\varepsilon-2/P^2)/\varepsilon_2$ and are therefore impossible. Solutions of period 2π represent a ''figure-eight'' response and are not seen in experiments.

4 Dynamics Discussion

4.1 Scan Distortion Prediction. One of the main goals of deriving a system model for the scanner was to understand the dynamic behavior that leads to distortion in the scan—an amplitude dependent phase shift, nonlinear amplitude response, jump, and whirl. Also, the nonlinear state space model (Eqs. 11*a*-11*d*) must be able to predict these distortion-causing dynamics, if a controller to remove the distortion is to use them.

Examining, the planar amplitude frequency response of the Duffing equation with centripetal acceleration for a rater scan (Eq. 15*a*), the solutions to A_z are nonlinear in F, which accounts for the nonlinear amplitude response. The planar phase frequency response (Eq. 15*b*) shows the phase varies with amplitude A_z due to aerodynamic drag but also inversely with amplitude square, A_z^2, due to the cubic nonlinearity. This accounts for the amplitude dependent phase shifts. From Eq. 15*a*, the amplitude response of the planar Duffing equation with centripetal acceleration for a raster scan is a sixth order polynomial in A_z. Because A_z must be positive, there are up to three possible responses—two stable and one unstable. In regions away from resonance, of the three solutions, only one real-valued solution exists; the other two solutions are imaginary valued. Since the response can be multi-valued, the Duffing equation with centripetal acceleration is able to describe the jump phenomena. *Section 3.3 Stability of the Raster Scan's Out-of-Plane Response* showed that the Duffing equation with centripetal acceleration is able to predict whirl for the raster scan.

Notice, the amplitude frequency response for a spiral and propeller scans when $\omega_y=1$ and $A=A_z=A_y$ (Eq. 17 and Eq. 19 respectively), have a similar form to the raster scan's planar frequency response (Eq. 15*a*) except different groupings of the nonlinear spring, ε, and centripetal acceleration, ε_2, coefficients. Because their amplitude dependencies are the same as the raster scan's, the spiral and propeller scans are also predicted to exhibit the nonlinear amplitude response, the amplitude dependent phase response, and jump.

4.2 Equivalent Nonlinear Spring Coefficients. Examining the planar frequency response of the Duffing equation with centripetal acceleration (Eq. 15*a*), the centripetal acceleration effect ε_2 is grouped with the nonlinear spring effect ε and has the same amplitude dependence. Because they have nearly the same effect near resonance, $\Omega\approx1$, it would be difficult to determine the values of the individual coefficients ε and ε_2 from the frequency response curves, but the combination ε_{equiv} can be found. Like equivalent viscous damping, an argument can be made to find an equivalent effective nonlinear spring coefficient for the group whose effect is the same averaged over the cycle.

$$\frac{3}{4}\varepsilon_{equiv.raster}=\frac{3}{4}\varepsilon+\frac{1}{4}\Omega^2\varepsilon_2\rightarrow\varepsilon_{equiv.raster}=\varepsilon+\frac{1}{3}\Omega^2\varepsilon_2. \tag{26}$$

The equivalent nonlinear spring coefficient is independent of amplitude and proportional to the square of the frequency. Since only frequency ranges near resonance $\Omega\approx1$ are considered, the coefficient is nearly constant.

By using the equivalent nonlinear spring coefficient, the Duffing equation can be used without the inclusion of the centripetal acceleration.

$$\ddot{p}+\varepsilon b\dot{p}+\varepsilon\alpha|\dot{p}|\dot{p}+p=-\varepsilon_{equiv}p^3+\varepsilon CF\cos\Omega t \tag{27}$$

with frequency-amplitude response of

$$\left(\varepsilon b\Omega+\frac{8}{3\pi}\varepsilon\alpha\Omega^2A\right)^2+\left(\frac{3}{4}\varepsilon_{equiv}A^2+1-\Omega^2\right)^2=(\varepsilon CF/A)^2 \tag{28}$$

with $\varepsilon_{equiv.raster}=\varepsilon_{equiv}=\varepsilon+1/3\Omega^2\varepsilon_2$ for the raster scan.

This is applicable only to a raster scan and only when whirl is not present. With whirl present, the y-dynamics have several groupings of ε and ε_2: $(1/4\varepsilon+3/4\varepsilon_2\Omega^2)$, $(1/4\varepsilon-1/4\varepsilon_2\Omega^2)$, and $(3/4\varepsilon+1/4\Omega^2\varepsilon_2)$. The equivalent nonlinear spring coefficient cannot be used. However, when using control algorithms with a raster scan, whirl would be removed [2] and therefore the response would again follow that of the planar Duffing equation. Therefore, the Duffing equation with equivalent nonlinear spring coefficient can be used to design and implement controllers for the raster scan.

Similarly, the spiral scan's frequency response (Eq. 17) looks similar to that of the Duffing equation (Eq. 28) except that the parameter for the nonlinear geometric effects is $(\varepsilon+\varepsilon_2\Omega^2)$ instead of $3/4\varepsilon$. An equivalent nonlinear spring coefficient can be found for the combination of the two nonlinear geometric effects.

$$\frac{3}{4}\varepsilon_{equiv.raster}=\varepsilon+\varepsilon_2\Omega^2\rightarrow\varepsilon_{equiv.raster}=\frac{4}{3}(\varepsilon+\Omega^2\varepsilon_2) \tag{29}$$

The centripetal acceleration appears to have a larger contribution to the combination in the spiral case than in the raster case. The coefficients ε and ε_2 are weighted in a 3:1 ratio in the raster case but in a 1:1 ratio in the spiral case.

Again it would be difficult to determine the individual coefficients ε and ε_2 from the frequency response curves. However, if we use both the equivalent nonlinear spring coefficients from the raster scan and the spiral scan, we have two equations and two unknowns. Using Eqs. 26 and 29, solving for ε and ε_2, and letting $\Omega\approx1$ yield

$$\varepsilon=\frac{3}{2}\varepsilon_{equiv.raster}-\frac{3}{8}\varepsilon_{equiv.spiral} \tag{30}$$

$$\varepsilon_2=-\frac{3}{2}\varepsilon_{equiv.raster}+\frac{9}{8}\varepsilon_{equiv.spiral} \tag{31}$$

Although the two coefficients can be determined, by using the equivalent nonlinear spring coefficient the Duffing equation can be used instead of Duffing equation with centripetal acceleration, but only for the corresponding scan pattern.

The propeller scan's frequency response (Eq. 17) looks similar to the Duffing equation's response (Eq. 28) except the nonlinear geometric effects have the effect of $3/2\varepsilon+1/2\Omega^2\varepsilon_2$ instead of $3/4\varepsilon$. An equivalent nonlinear spring coefficient can be found for the combination of the two nonlinear geometric effects. The propeller scan's equivalent nonlinear spring coefficient is twice that of the raster scan's.

$$\frac{3}{4}\varepsilon_{equiv:raster}=\frac{3}{4}\varepsilon+\frac{1}{4}\Omega^2\varepsilon_2 \tag{32}$$

$$\frac{3}{4}\varepsilon_{equiv:propeller}=\frac{3}{2}\varepsilon+\frac{1}{2}\Omega^2\varepsilon_2 \tag{33}$$

This is expected because the propeller scan without modulation is actually a raster scan with $\sqrt{2}$ times the forcing amplitude and rotated 45 deg. Because the equations are not linearly independent, the propeller scan's frequency response cannot be used in conjunction with the raster scan's to determine the individual coefficients ε and ε_2. Also, just as whirl occurs for the raster scan, whirl may occur for the propeller scan.

5 Experimental Measurements

Experiments were performed to confirm the appropriateness of the dynamic model for the fiber scanner and to determine the system parameters. The procedure can be summarized as follows:

• First, the profile of the fiber vibration near resonance was compared to the corresponding linear modeshape.

• The fiber's steady-state amplitude and phase responses due to sinusoidal base excitations were measured with least squares estimates. The responses were collected for a raster in the *z*-direction, raster scan in the *y*-direction, a spiral (circular) scan, and propeller (45 deg line) scan. For each scan pattern, the frequency responses were obtained for various input amplitudes.

• Parameters ω, $\varepsilon\alpha$, εb, εC, ε_{equiv} were chosen to find a good match between the analytic and experimental frequency responses. The linear parameters, ω, εb, and εC can be found in the frequency responses' linear regions either by eye or using a least squares technique. From the raster and spiral scans' ε_{equiv} parameters, which were found by visually fitting the bending over of the response curves, the coefficients ε and ε_2 were determined algebraically.

• The scaling factor, *s*, of the sensor was determined.

• Finally, the piezotube response was checked over the scans' frequency range and at several input amplitudes. A frequency response of the piezotube up to its first bending resonance was also collected to ensure a second-order system (bending tube) approximation and a proportional model are correct.

5.1 Experimental Setup. Figure 1 shows the experimental setup. Light from a diode laser (ThorLabs 635 nm model SIFC635) is coupled into a single-mode optical fiber (Spectran SMC-A0630B, 4 μm core diameter). Near the opposite end, the fiber is threaded through and glued to a 2 μL pipette that is further attached to a piezotube with quartered electrodes (PZT-5H, Valpey-Fisher) by a metal collet that acts as the base of the cantilever. The length of the fiber extending beyond the pipette and collet is stripped of its plastic protective buffer to reduce damping. The piezotube is mounted on a 3-axis micrometer positional stage. Two D/A outputs from a PCI-6111E data acquisition board (National Instruments) installed in a Macintosh G3 (Apple Computer) are controlled by LabView (National Instruments) to generate the horizontal and vertical waveforms (0V to $\pm$10V). These voltages are amplified by a 15$\times$ high-voltage amplifier ($V_{\max}=\pm 150$ V, $\omega_{-3db}=50$ kHz). The high-voltage amplifier outputs with 0 deg and 180 deg phase shifts are applied to opposite planar quadrants of the piezotube.

Light emanating from the vibrating fiber tip impinges on a dual-lateral two-dimensional position sensor (UDT Sensors, DL-10 photodiode). The sensor responses are amplified using a current to voltage preamplifier, an analog difference circuit, and a second amplifier stage. The sensor and piezotube with stages are enclosed in a box to reduce the amount of stray environmental light. The sensor is vertically mounted on a rotational stage to insure that the sensor axes are aligned with the vibration axes. The same PCI-6111E DAQ card uses four analog A/D converters to collect the *z*-axis and *y*-axis signals from the position sensor and the unamplified piezotube drive signals. The resulting waveforms are saved to a text file, which are then imported into Matlab (Mathworks), where signal analyses are performed. Intermediate results from Matlab and Simulink are saved to textfiles, which are then imported into MathCad (MathSoft) for further analysis.

5.2 Linear Mode Shapes. The fiber was excited into its second mode of resonance. A digital picture was taken of the deflection profile using a digital camera (Kodak DC290). Using MathCad, the second mode shape of the cantilever was computed using Eq. 4*b*,

$$\beta^4=\rho A\Omega^2/EI,$$

$$E=73.8\cdot 10^9 \text{ Pa} \quad \rho=2.203\cdot 10^3 \text{ kg/m}^3,$$

$$\Omega=305\cdot 2\pi \text{ rad/sec}, \quad l=45.27\cdot 10^{-3} \text{ m},$$

$$D=125\cdot 10^{-6} \text{ m}, \quad A=\frac{1}{4}\pi D^2, \quad I=\frac{1}{64}\pi D^4$$

Fig. 4 Resonating Fiber Profile and Theoretical Mode Shape

The mode shape plot and digital picture were loaded into Adobe Illustrator and the mode shape plot scaled until the amplitudes match. As seen from Fig. 4, the theoretical second mode shape (black and white dashed line) is in good agreement with the measured mode shape.

5.3 Scan Frequency Responses. To obtain the fiber's frequency response for the raster, spiral, and propeller scans, a LabView program outputs a constant amplitude and constant frequency drive sine wave plus an auxiliary complementary cosine wave, both sampled at 100,000 samples/second ($\sim$333 samples/cycle). The appropriate drive signal for the scan type is amplified and applied to the quadrants of the piezotube. The program waits until the fiber's vibrations reach steady-state, then samples the sensor's *z* and *y* outputs, and the sine and cosine functions at 40,000 samples/second for 0.5 s ($\sim$67 cycles). The four waveforms are saved as a file. The program then changes the frequency keeping the drive amplitude constant and the process repeats over the desired frequency range forming one run. Several runs are made each with different constant drive amplitudes of 2, 4, 6, 8, and 10 volts, before amplification.

The waveform files are imported one at a time into Matlab, where a least squares parameter identification Simulink model uses the sine and cosine waves as basis functions to give the best estimates of the amplitude and phase of the *z* and *y* response. The frequency, amplitude and phase are stored in an array and the aggregate frequency response of each run saved as a text file. By using least-squares parameter identification of the amplitude and phase, the amplitude and phase measurements become robust to noise and human error.

The experimental frequency response files were imported into a MathCad file where they are plotted along with the theoretical frequency response, remembering the theoretical frequency response is given in terms of normalized *z* frequency. The parameters, ω, $\varepsilon\alpha$, εb, εC, ε_{equiv} were chosen until a good visual match between the experimental and theoretical frequency response was achieved for a given drive amplitude. The drive amplitude was then changed to ensure the frequency responses still matched over the entire drive amplitude range.

To determine the scaling of the sensor, the piezo actuation was removed, and the micrometer was moved a known amount and the change in voltage noted. The sensor scaling factor was 0.3185 mm/V.

5.3.1 Raster Scans-z and y Directions. For a raster scan in the *z*-axis (*z*-raster), a sine wave signal is amplified and applied to the vertical opposite planar quadrants of the piezotube. For a *z*-raster scan the following parameters provided a good visual match:

$$\omega_z=304.481 \text{ Hz}, \quad \varepsilon\alpha=0.004, \quad \varepsilon b=0.011,$$

$$\varepsilon_{equiv.raster}=-0.007, \quad \varepsilon C\cdot f_v=0.00083$$

$$f_2=0.82, \quad f_4=0.85, \quad f_6=0.9, \quad f_8=0.95, \quad f_{10}=0.99$$

where f_v is a drive amplitude dependant (v) scaling factor that accounts for any amplitude nonlinearity in the piezotube (deviations from the proportional actuator assumption).

From the spiral scan (described below), the equivalent nonlinear spring coefficient was found to be $\varepsilon_{equiv.spiral}=0.0012$. Using the equivalent nonlinear spring coefficients for the raster scan and the spiral scan, and their known relationships (Eqs. 30, 31), we can solve for the parameters ε and ε_2.

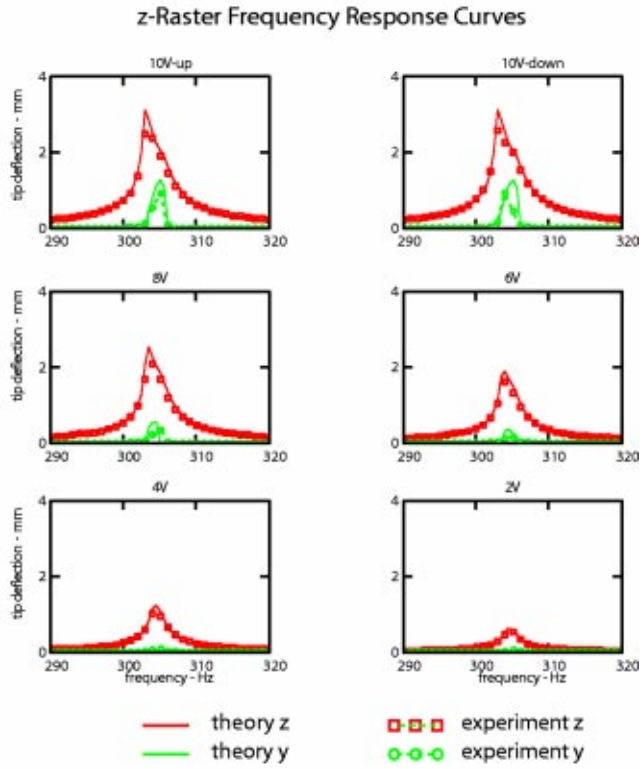

Fig. 5 *z*-Raster frequency response curves for 2,4,6,8,10 Volts—Theory vs. Experiment

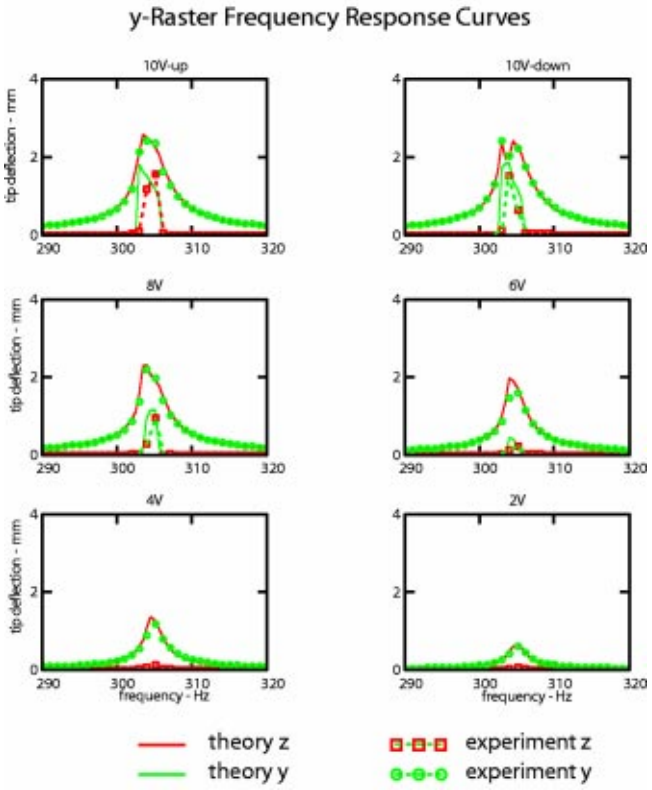

Fig. 6 *y*-Raster frequency response curves for 2,4,6,8,10 Volts—Theory vs. Experiment

$$\frac{3}{4}\varepsilon_{equiv.raster} = -0.007 = \frac{3}{4}\varepsilon + \frac{1}{4}\varepsilon_2 \tag{34}$$

$$\frac{3}{4}\varepsilon_{equiv.spiral} = 0.0012 = \varepsilon + \varepsilon_2 \tag{35}$$

$$\varepsilon = -0.011, \quad \varepsilon_2 = .0123$$

Fig. 5 shows the predicted *z*-raster cross-coupled frequency response (Eqs. 14*a*,*b*) from 290 Hz to 320 Hz at 2,4, . . . 10 volts (before amplification) with experimental results overlaid. The same procedure was used for a raster scan in the *y*-axis (*y*-raster). For a raster scan in the *y*-axis (*y*-raster), a sine wave signal is amplified and applied to the horizontal opposite planar quadrants of the piezotube.

Figure 6 shows the predicted *y*-raster cross-coupled frequency response from 290 Hz to 320 Hz at 2,4, . . . 10 volts (before amplification) with selected experimental results overlaid. Only ω_y and f were allowed to differ from the *z*-raster values. A good match was still possible with the following parameter values: $\omega_y = 304.897$ Hz and $f_2 = 0.86$, $f_4 = 0.9$, $f_6 = 0.94$, $f_8 = 0.97$, $f_{10} = 1.01$.

The difference in natural frequencies in the *z* and *y*-directions are easily apparent from the responses. The frequency ratio of the two axes natural frequencies is $\omega_y/\omega_z = 1.001$.

5.3.2 Spiral Scan Frequency Response. To obtain the fiber's frequency response for a spiral scan a sine wave signal is amplified and applied to the vertical opposite planar quadrants of the piezotube. Likewise, the cosine wave signal is amplified and applied to the horizontal opposite planar quadrants. From the frequency response, the equivalent nonlinear spring coefficient was found to be $\varepsilon_{equiv.spiral} = 1.2 \cdot 10^{-3}$. Using the equivalent nonlinear spring coefficients for the raster scan and the spiral scan, and their known relationships (Eqs. 30, 31), we can solve for the parameters ε and ε_2. $\varepsilon = -1.1 \cdot 10^{-2}$, $\varepsilon_2 = 1.23 \cdot 10^{-2}$.

Figure 7 shows the experimental and predicted spiral frequency response of the fiber in second mode of resonance from 290 Hz to 320 Hz at 2,4, . . . 10 volts (before amplification). The full set of four implicit equations in A_z, A_y, ϕ_2, ϕ_3 (Eqs. 13*a*–*d*) with $v_z = F\cos\Omega t$ and $v_y = F\sin\Omega t$ was used to determine the predicted frequency response.

The same values for ω_z, ω_y $\varepsilon\alpha$, εb, ε, ε_2 and $\varepsilon C \cdot f$ used in the raster scan were used here. The same small variations in the forcing constant f in the *z* and *y*-axis used in the raster scan were used here.

5.3.3 Propeller Scan Frequency Response. To obtain the fiber's frequency response for a propeller scan, a sine wave signal is amplified and applied to the vertical opposite planar quadrants of the piezotube. Likewise, a sine wave signal is amplified and applied to the horizontal opposite planar quadrants. Figure 8 shows the experimental and predicted frequency response of the fiber in second mode of resonance from 290 Hz to 320 Hz at 2,4, . . . 10 volts (before amplification). The full set of four implicit equations in A_z, A_y ϕ_2, ϕ_3 (Eqs. 13*a*-*d*) with $v_z = F\cos\Omega t$ and $v_y = F\cos\Omega t$ was used to determine the predicted frequency response. The same values for ω_z, ω_y, $\varepsilon\alpha$, εb, ε, ε_2 and $\varepsilon C \cdot f$ used in the raster scan were used here. The same small variations in the forcing constant f in the *z* and *y*-axis used in the raster scan were used here.

5.4 Piezotube Response. To determine the piezo response within the resonant frequency range of the fiber, the fiber was cleaved at the tip of the pipette. By doing this, we could determine the base motion without the fiber dynamics. The tip of the pipette was placed close to the dual-lateral position sensor and a frequency response was collected from 290 Hz to 320 Hz. Figure 9*a* shows the frequency response of the piezotube from 10 Hz to 10,000 Hz and the theoretical frequency response of a linear second order system. Figure 9*b*,*c* shows the piezotube's amplitude

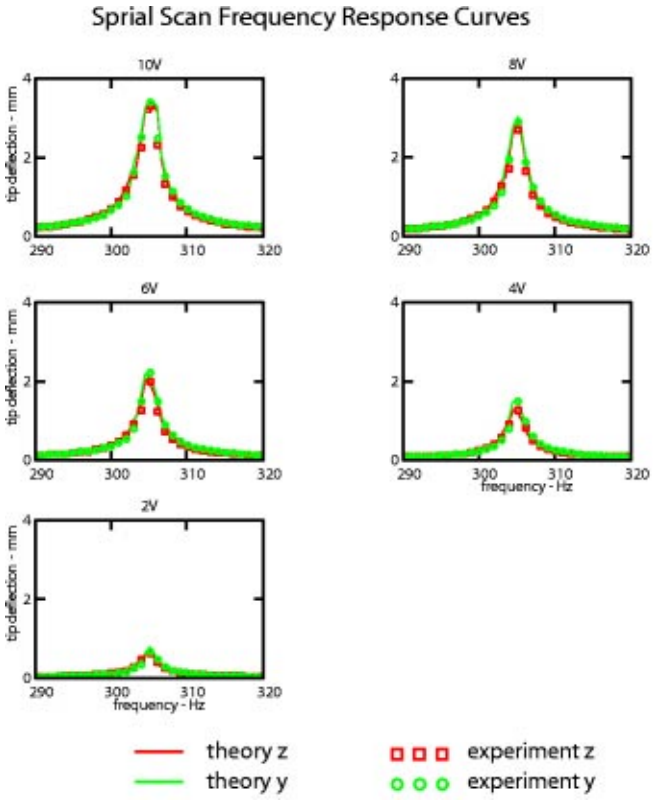

Fig. 7 Spiral scan frequency response curves for 2,4,6,8,10 Volts—Theory vs. Experiment

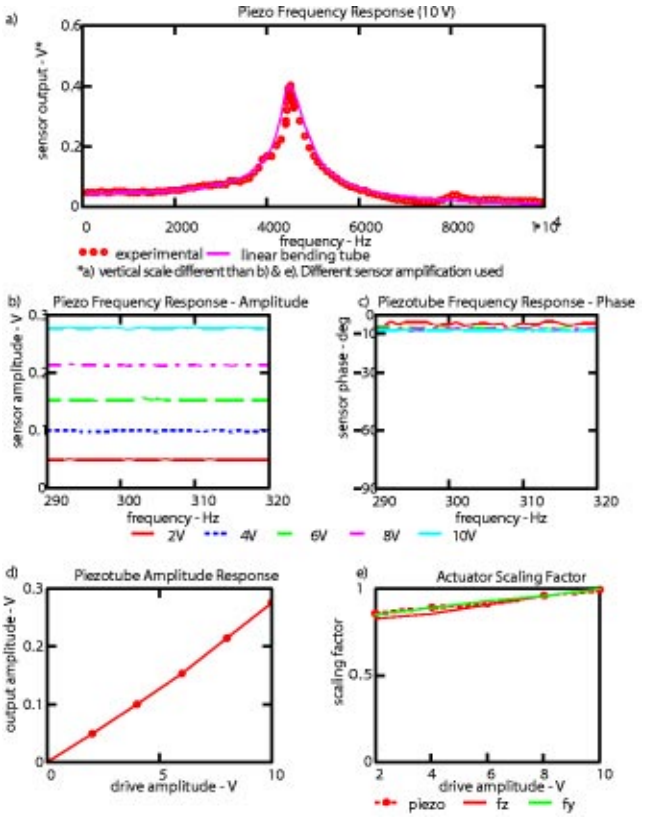

Fig. 9 Piezotube Frequency and Amplitude Response. *a*) Frequency Response 0-10,000 Hz. *b*), *c*) Amplitude and Phase Frequency Response near fiber resonance, *d*) Amplitude Response near fiber resonance, *e*) scaling factor vs amplitude

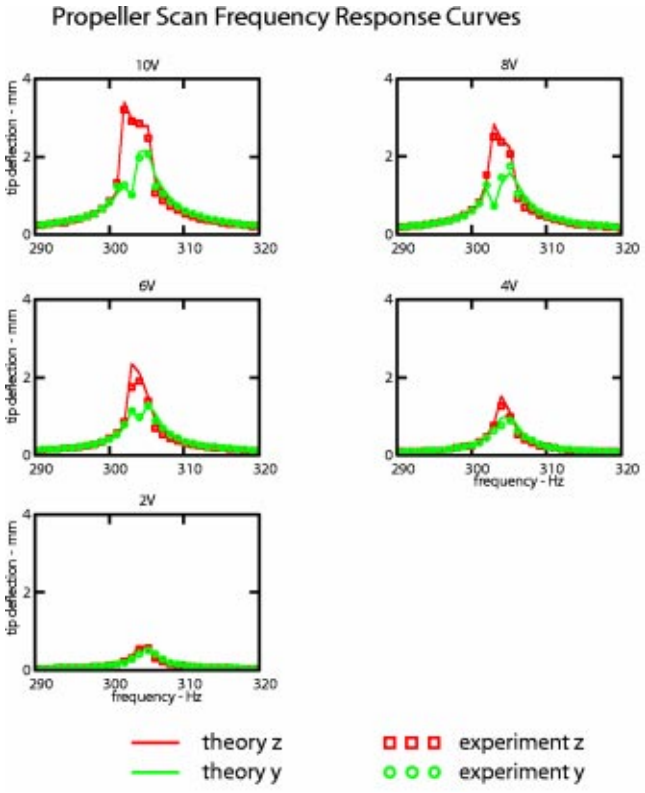

Fig. 8 Propeller scan frequency response curves for 2,4,6,8,10 Volts—Theory vs. Experiment

and phase frequency response from 290–320 Hz at 2, 4, . . . 10 volts (before amplification). Figure 9*d* shows the amplitude response of the piezotube at 300 Hz at 2, 4, . . . 10 volts (before amplification). Figure 9*e* shows the piezo amplitude variation with the fiber system's amplitude variation, f_v, normalized with respect to the largest amplitudes.

6 Experimental Results Discussion

6.1 Mode Shapes. As seen from Fig. 4, the theoretical linear second mode shape (black and white dashed line) is in good agreement with the actual mode shape. Because linear mode shapes can be used to describe the fiber's deflection curve even while undergoing moderate displacements, the linear mode shapes can be used in conjunction with an inextensibility constraint to determine the fiber's tip position and angle throughout its vibration [16]. The mode shape can be integrated along its path length until a fixed value—the fiber's rest length—is accumulated. At that station—the tip position—the displacement and angle can be determined. The fiber tip position and angle throughout its vibration is useful in designing the optics to minimize aberrations [16].

6.2 System Frequency Responses

6.2.1 Parameter Values. For the nonlinear state-space dynamics

$$\ddot{p}+\varepsilon b\dot{p}+\varepsilon\alpha\dot{p}|\dot{p}|+p=-\varepsilon p(p^2+q^2)-\varepsilon_2 p(\dot{p}^2+\dot{q}^2)+\varepsilon C f_v v_z \tag{12a}$$

$$\ddot{q}+\varepsilon b\dot{q}+\varepsilon\alpha\dot{q}|\dot{q}|+\omega_y^2 q=-\varepsilon q(p^2+q^2)-\varepsilon_2 q(\dot{p}^2+\dot{q}^2)+\varepsilon C f_v v_y \tag{12b}$$

the following parameter values were determined from the experiments:

$$\omega_z = -304.481\ Hz, \quad \omega_y = 304.897\ Hz, \quad \varepsilon\alpha = 0.004,$$

$$\varepsilon b = 0.11, \quad \varepsilon = -0.011, \quad \varepsilon_2 = .0123, \quad \varepsilon C \cdot f_v = 0.00083.$$

$$f_2 = 0.82, \quad f_4 = 0.85, \quad f_6 = 0.9, \quad f_8 = 0.95, \quad f_{10} = 0.99$$

for the *z*-axis piezo quadrants

$$f_2 = 0.86, \quad f_4 = 0.9, \quad f_6 = 0.94, \quad f_8 = 0.97, \quad f_{10} = 1.01$$

for the *y*-axis piezo quadrants

The parameters were chosen to give a good visual fit of the frequency response equations to the experimental frequency responses. A systematic procedure for determining the model parameters is given below. Because damping and nonlinear dynamic effects (nonlinear spring and centripetal acceleration effects) are not significant at frequencies away from resonance, the natural frequency ω_z and forcing constant $\varepsilon C \cdot f_v$ (with $f_v = 1$) parameters dominate in the frequency ranges 290 Hz–300 Hz and 310 Hz–320 Hz. Because whirl does not occur at frequencies away from resonance, the theoretical planar Duffing equation's frequency response (Eq. 28) can be used with the *z*-raster's experimental frequency response at 10-volts (Fig. 5) to determine ω_z and $\varepsilon C \cdot f_v$. The parameter values are varied until the theoretical and experimental responses visually match in the frequency ranges 290 Hz–300 Hz and 310 Hz–320 Hz. In the theoretical planar Duffing equation's frequency response, the parameters εb, $\varepsilon\alpha$, ε are set to arbitrary values, and the nonlinear spring coefficient ε is considered to be the equivalent nonlinear spring coefficient for the raster scan, $\varepsilon_{equiv.raster}$. The values of the piezotube's scaling factor $f_{v,z}$ for the z-axis can then be found by using the z-raster's frequency response curves at the piezotube's voltages of 2,4, . . . ,8 volts in the frequency ranges 290 Hz–300 Hz and 310 Hz–320 Hz and determining $f_{v,z}$ for each voltage to provide a good visual fit. This assumes the scaling factor is constant over the frequency range of interest. For a linear piezotube response, $f_{v,z} = 1$ for all input voltages. At small piezotube voltages, and hence small base excitations and small tip displacements, internal (viscous) damping dominates aerodamping and the fiber acts in its linear dynamic range. The viscous damping term, εb, can be found by matching the resonant peak and width in the frequency range 300 Hz–310 Hz of the 2 volt and 4 volt *z*-raster theoretical (Eq. 27) and experimental frequency response curves (Fig. 5). Although the linear parameters can alternatively be found more precisely and simultaneously using frequency response data away from the resonant region and a least squares parameter estimation technique (see section 6.2.2), extremely precise parameter values are not absolutely required because the controller will be robust to modest parameter variations. The equivalent nonlinear spring coefficient, $\varepsilon_{equiv.raster}$, can be found by using the 6, 8, or 10-volt frequency response curves and varying $\varepsilon_{equiv.raster}$ until there is a good visual match of the bending over of the curves in regions where whirl does not occur or does not significantly affect the in-plane response. At these higher voltage response curves, aerodamping becomes significant and its parameter value, $\varepsilon\alpha$, can be found by and making a good visual match at the resonant peak.

The planar Duffing equation (Eqs. 27 and 28) in conjunction with the experimental *y*-axis frequency responses are used to determine the *y*-axis natural frequency, ω_y, and the values of the piezotube's scaling factor $f_{v,y}$ for the *y*-axis. Again, in the frequencies away from resonance, 290 Hz–300 Hz and 310 Hz–320 Hz, the natural frequency ω_y and forcing constant $\varepsilon C \cdot f_v$ parameters dominate. We assume the forcing constant εC without the piezotube's scaling factor f_v has the same value in the *y*-direction as it does in the *z*-direction for an isotropic fiber. We determine the *y*-axis natural frequency, ω_y, to account for any slight asymmetry in the fiber. Due to manufacturing variability, the piezotube's scaling factor may be different in the *z*-direction and the *y*-direction.

The spiral scan's experimental frequency responses and the simplified frequency response (Eq. 17), with Eq. 35 ($3/4\varepsilon_{equiv.spiral} = \varepsilon + \varepsilon_2\Omega^2$) can be used to determine the $\varepsilon_{equiv.spiral}$ by matching the bending over of frequency response curves at higher voltages. The simplified spiral frequency responses (Eq. 17) can be used because the experimental results (Fig. 7) show that $A_z \cong A_y$. Because the response is a single implicit equation, MathCad's implicit equation solver (Given, Find) gives quick, accurate results. From the combination of $\varepsilon_{equiv.raster}$ and $\varepsilon_{equiv.spiral}$, the nonlinear spring coefficient, ε, and the centripetal acceleration coefficient, ε_2, can be found using Eqs. 30 and 31. Hence, all the parameter values for the system dynamic model (Eqs. 12*a*,*b*) can be determined in a simple systematic manner, one parameter at a time, using various simplified frequency response equations. Since the parameter values for the experimental system have been determined, we can determine how well the full set of four implicit equations predicts the system response, not just at the points used in the parameter identification, but also for the entire frequency response, for different forcing values, and for different scan types, including whirl and the propeller scan, both of which were not used for parameter identification. If the full model with a single set of parameters is able to predict the system response for various scan patterns at various amplitudes, we can place faith in the model that it will be able to predict the response for a general excitation as might be seen in a controls application.

6.2.2 Raster Scan Frequency Response. For the *z*-raster and *y*-raster scans, we are interested in the ability to predict the bending over of the frequency response curve at various amplitudes, and the range and amplitude of the non-planar response (whirl). We use the frequency responses for the cross-coupled Duffing equation with centripetal acceleration and aerodamping for a raster scan (Eqs. 14*a*,*b*). When whirl is present, the solution of the implicit equation solver is sensitive to initial guesses and may not converge to consistent values leading to imprecise ''noisy'' solutions.

Figure 5 shows the predicted *z*-raster cross-coupled frequency response from 290 Hz to 320 Hz at 2,4, . . . 10 volts (before amplification) with experimental results taken at whole frequencies (290,291, . . . 320 Hz) overlaid. The in-plane predicted response matches the experimental measurements quite well, but the out-of-plane (whirl) predicted results are slightly overestimated. The experimental whirl shape is different when the frequency is swept from 290 Hz to 320 Hz than when swept from 320 Hz to 290 Hz. The whirl frequency range is predicted correctly; however, the whirl shape is accurately predicted when the frequency is swept upwards, but not when swept downwards. Whirl is not predicted at amplitudes less than 6 V due to damping, however an out-of-plane response is experimentally measured at 4 V and 2 V. This out-of-plane response is most likely a slight misalignment in the sensor.

Figure 6 shows the predicted *y*-raster cross-coupled, frequency response from 290 Hz to 320 Hz at 2,4, . . . 10 volts (before amplification) with experimental results overlaid. A small variation in the forcing constant εC provides a good fit. The difference in natural frequencies in the *z* and *y*-directions is readily apparent by the shift in the response curve, which is consistent at all forcing amplitudes. The frequency ratio of the two axes natural frequencies is $\omega_y / \omega_z = 1.001$.

The out-of-plane results for the *y*-raster frequency response match the experimental measurements in width and height. The whirl shape is different when the frequency is swept upwards from 290 Hz to 320 Hz than when swept downwards from 320 Hz to 290 Hz. The whirl frequency range is predicted correctly; however, the predicted whirl shape matches for the downward sweep but is opposite for the upward frequency sweep. Again, whirl is not predicted at amplitudes less than 6 V due to damping and the out-of-plane response seen at 4 V and 2 V is most likely a slight misalignment in the sensor.

Although the whirl amplitude is slightly overestimated in the *z*

and *y*-raster, the general frequency range and shape is predicted well. When using control algorithms with a raster scan, the whirl instability is regulated and not allowed to grow [2], and therefore the slight disparity is not significant. The general frequency range and shape are sufficient.

The planar amplitude frequency response for a raster scan (Eq. 15*a*) was derived from the general frequency response equations (Eqs. 13*a-d*, $F_y=0$, $A_y=0$). The phase response for the planar Duffing equation with centripetal acceleration (Eq. 15*b*) was also found using the same secular equations. Since both the amplitude and phase responses are derived from the same secular equations, experimental confirmation of the amplitude frequency response equations implies the ability to accurately predict the phase response. Collection of the phase response, therefore, gives no additional information, and experimental phase responses were not collected.

The experimental data was collected at unit frequency intervals (290Hz, 291Hz . . . 320Hz), resulting in sparse data near the resonant peak (about ten points) and whirl region (about four points) at each voltage. There are however, five or six voltage values examined per scan type and the same parameters are used for all four scans types. Therefore, there are effectively eighty-eight points (whirl) to 220 data points (resonant peak) to determine how well the model and data fit in the resonant region. Furthermore, because the frequency response is governed by seven parameters and varies piecewise smoothly, dense data does not necessarily provide more information on parameter estimation or the goodness of fit. For instance, the linear mass-spring damper, $\ddot{p}+b\dot{p}+\omega^2 p=CF\cos\Omega t$ has a frequency response of $b^2\Omega^2+(\omega^2-\Omega^2)^2=(CF/A)^2$ which can be rewritten as a linear relation $y=D\theta$:

$$1/A^2=[\Omega^4 \quad \Omega^2 \quad 1]\cdot[(CF)^{-2} \quad (b^2-2\omega^2)(CF)^{-2} \quad \omega^4(CF)^{-2}]^T \tag{36}$$

Given data points (Ω,A) for a given force F, this relation can be solved for the parameters, θ, using a linear least-squares technique. Thus only three data points are needed to uniquely determine the three model parameters, ω, b and C, although additional data points add noise robustness.

As seen in *Section 6.2.1 Parameter Values*, a systematic means of determining the parameter values for our nonlinear system was developed, only four of which, εb, $\varepsilon\alpha$, $\varepsilon_{equiv.raster}$ and $\varepsilon_{equiv.spiral}$, depend on the resonant region and none on whirl. The parameters εb and $\varepsilon\alpha$ use various voltages from each scan and can be crosschecked (assuming consistency) between the *z*-raster, *y*-raster, spiral and propeller scans. $\varepsilon_{equiv.raster}$ is determined using the *z*-raster and *y*-raster scans using at least three voltage plots in each, and $\varepsilon_{\text{equiv.spiral}}$ is found using the spiral scan using at least three voltage plots. The combination of $\varepsilon_{equiv.raster}$ and $\varepsilon_{equiv.spiral}$ give the nonlinear spring coefficient, ε, and the centripetal acceleration coefficient, ε_2. Thus, these two coefficients use almost sixty points (six plots with 10 points per plot) to determine their values.

Figure 10*a* shows the predicted linear frequency response for the raster scan, as well as the planar frequency response with and without centripetal acceleration. Clearly, the nonlinear spring and centripetal acceleration terms are needed to accurately predict the bending over of the frequency response curve for the raster case. Centripetal acceleration causes a 'hardening' effect, without which the nonlinear response (due only to the nonlinear spring) would bend more to the left.

Although jump is not clearly exhibited in these experiments, other tests have shown a good prediction of the jump phenomena. The experiments reported here can accurately predict the bending over of the frequency response. Since, jump occurs when the bending is sufficient to allow multi-valued solutions at a given frequency, we expect the ability to accurately predict any jumps that occur in experiments. It is worth noting that the quality and method of coupling affects the nonlinear response greatly. Small variations can show large changes in the output response including the appearance of whirl and jump even at small amplitudes. Ray and Bert, Wrenn and Mayers, and Nayfeh ([17], pg. 453) found that a spring support reduces the effect of the nonlinearity. This is an additional reason for experimentally determining the parameters rather than predicting their values from physical quantities such as stiffness, density, moment of inertia and so on.

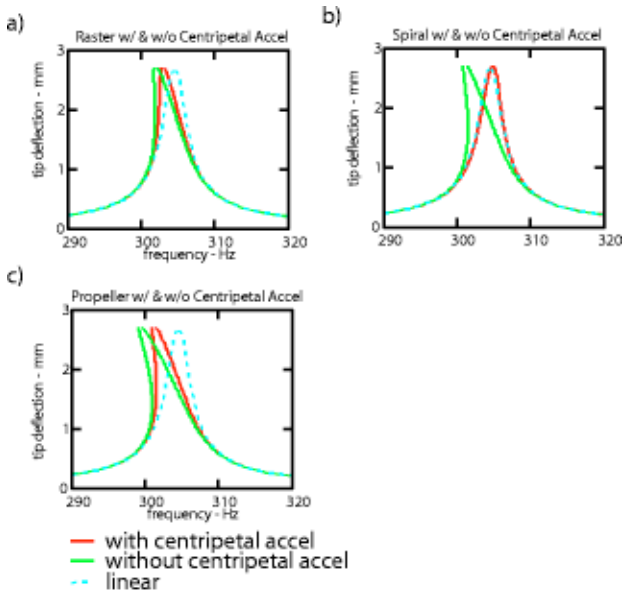

Fig. 10 Frequency Response Plots with and without Centripetal Acceleration and Linear Response

6.2.3 Spiral Scan Frequency Response. Figure 7 shows the experimental and predicted spiral frequency response of the fiber in second mode of resonance from 290 Hz to 320 Hz at 2,4, . . . 10 volts (before amplification). The full set of four implicit equations in A_z, A_y, ϕ_2, ϕ_3 (Eqs. 13*a–d*) with $v_z=F\cos\Omega t$ and $v_y=F\sin\Omega t$ was used to determine the predicted frequency response because experiments show that $A_z\neq A_y$ near resonance (see Fig. 7). The implicit equation solver requires initial guesses for A_z, A_y, ϕ_2, ϕ_3. Below the resonant region, 290 Hz–300 Hz, we expect $\phi_2=0$, $\phi_3=0$. Above the resonant region, 310 Hz–320 Hz, we expect, $\phi_2=\pi$, $\phi_3=\pi$. Within the resonant region, 300 Hz–310 Hz, we expect the ϕ_2, ϕ_3 to vary between 0 and π with $\pi/2$ often being a good initial guess. In this region, we don't expect ϕ_3 to always equal ϕ_2 due to the different resonant frequencies in the *z* and *y*-axes. For the amplitude guesses, A_z, A_y, we can choose values close to the experimental data values. Various guesses of A_z, A_y, ϕ_2, ϕ_3 are made until a good visual match is found.

For a majority of the frequency response, the responses in both axes, A_z and A_y, are identical. In a small region just below the maximum amplitude, they differ. This is most likely due to a slight difference in the resonant frequencies of the two axes. The model is able to accurately account for the subtle differences in the two axes' responses due to the different resonant frequencies. For the spiral scan, the frequency response curve bends towards the higher frequencies, opposite the bending of the frequency response curve for the raster scan. Fig. 10*b* shows the predicted linear frequency response and nonlinear frequency responses with centripetal acceleration ($\varepsilon=-0.011,\varepsilon_2=.0123$) and without centripetal acceleration ($\varepsilon=-0.011,\varepsilon_2=0$) for the spiral scan using the simplified frequency response (Eq. 16). Centripetal acceleration plays an important role in the spiral scan response. From the analytic results, without centripetal acceleration we would expect the response curve to bend over further towards the lower frequencies than the raster scan because the spiral's effective nonlinear coefficient should have increased by 4/3 over the raster scan. As mentioned, an effect of centripetal acceleration is to change the

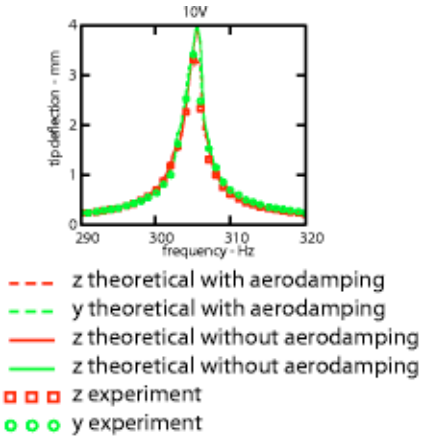

Fig. 11 Spiral Scan Frequency Response with and without aerodynamic damping

effective nonlinear spring coefficient $3/4\varepsilon_{equiv}=\varepsilon+\varepsilon_2\Omega^2$ in the cross coupled Duffing equation without centripetal acceleration. The centripetal acceleration adds a 'hardening' spring effect, which bends the response curve to the right. For the raster scan and propeller scan, the difference with and without centripetal acceleration is not as significant, comparing Fig. 10*b* to Figs. 10*a*,*c*.

From Fig. 10*b*, it also appears that the frequency response for the spiral scan is almost linear, so it would appear the inclusion of the nonlinear terms are unnecessary. Caution must be taken because this plot is only valid if $A_z=A_y$ and $\phi_2=\phi_3$. Experiments show that $A_z\neq A_y$, (Fig. 7) and other experiments using other fibers show a stronger hardening effect. As stated earlier, the quality and method of coupling affects the nonlinear response greatly, so it just by coincidence that the response is nearly linear. Furthermore, a linear model cannot predict the amplitude dependent amplitude and phase shifts, which create distortion in the images. Also, a linear approximation would not capture any of the cross-coupling between the axes.

Figure 11 shows the predicted nonlinear response without aerodamping. Aerodamping mainly affects the height of the resonant peak. Away from the resonant peak, it appears to have little effect. Aerodamping does not appear to contribute a majority of the damping, however it is necessary to provide the best fit over the amplitude range. If aerodamping is replaced by an equivalent viscous damping term, the frequency response may still be well predicted with the added benefit of the omission of a nonlinear term. The effects of this omission may become apparent in the dynamic response of the system submitted to nonsinusoidal forcing, and therefore must be kept in mind. Operating the fiber in an evacuated chamber and comparing the frequency response in vacuum to that in air is the best way to verify these results.

6.2.4 Propeller Scan Frequency Response. Figure 8 shows the experimental and predicted propeller frequency response of the fiber in second mode of resonance from 290 Hz to 320 Hz at 2,4, . . . 10 volts (before amplification). The full set of four implicit equations in A_z, A_y, ϕ_2, ϕ_3 (Eqs. 13*a*–*d*) with $v_z=F\cos\Omega t$ and $v_y=F\cos\Omega t$ was used to determine the predicted frequency response because the experimental frequency response clearly shows $A_z\neq A_y$. See Fig. 8. Hence, the propeller scan's simplified frequency response (Eq. 19) cannot be used. Like the spiral scan, the implicit equation solver requires initial guesses for A_z, A_y, ϕ_2, ϕ_3, with initial guesses made in a similar manner for different regions around resonance. Away from resonance, the responses in both axes are identical. Near resonance they vary greatly. This is most likely due to whirl. As stated earlier, the propeller scan without amplitude modulation is basically a raster scan with $\sqrt{2}$ times the forcing amplitude and rotated 45 deg. The raster scan exhibited whirling, so it is not surprising that the propeller scan does as well. The model is able to accurately account for the large differences in the two axes responses due to the different resonant frequencies and cross-coupling, where as a linear model would be unable to predict this. The good visual match between the predicted and experimental data is also impressive because the propeller scan was not used to determine the system parameters and is therefore a purely predicted response. As predicted from Eqs. 32 and 33, the equivalent nonlinear spring coefficient for the propeller scan is approximately twice that of the raster scan's as seen in the regions where the amplitudes are nearly identical and this evaluation is valid.

6.3 Piezotube Response. Figure 9*a* shows the frequency response of the piezotube from 10 Hz to 10,000 Hz and the theoretical frequency response of a linear second-order system. Below 6,000 Hz, the piezotube does behave like a bending-tube with a resonant frequency of about 4,500 Hz. There appears to be a softening spring nonlinearity of the piezotube at its resonance, but this nonlinearity and the piezotube's damping do not significantly affect the frequencies away from its resonance. There also appears to be a slight resonant peak at 8,000 Hz.

Figures 9*b*,*c* shows the amplitude and phase frequency response of the piezotube from 290 Hz to 320 Hz at 2,4, . . . 10 volts (before amplification). Over the frequency range of interest, the frequency response is almost flat and the input/output phase is nearly constant. The phase at 2 volts is slightly lower than at other voltages, but this is most likely due to noisy estimation errors of small piezo response. The phase shift seen from 290 Hz to 320 Hz is approximately 6 deg. The phases shift predicted by the second order system response is about 0.47 deg.

Figure 9*d* shows the amplitude response of the piezotube at 300 Hz at 2,4, . . . 10 volts (before amplification). The response is nearly linear, with a slight softening effect. This accounts for the variation of εC in the fiber's frequency response, represented by *f*. Figure 9*e* shows the piezo amplitude variation from a linear response and the scanning system's amplitude variation, *f*, normalized with respect to the largest amplitudes. For a perfectly linear amplitude response, $f=1$. The visual match is quite good for f_z, and excellent for f_y. Although the piezotube does show a dynamic nonlinear spring response, this is not the cause of the nonlinear amplitude response near resonance because the operating frequencies are far away from the piezotube resonance.

Most likely, the phase shift and nonlinear amplitude response is due to the hysteresis in the piezotube. Hysteresis for a piezotube can be modeled as a backlash nonlinearity at the input of the bending tube [12]. From the phase angle of the describing function for a backlash nonlinearity, a 6 deg phase lag corresponds to a backlash width to amplitude ratio, b/A, of 0.1 (a very narrow hysteresis curve). A backlash nonlinearity with $b/A=0.1$ is accompanied by an approximately 0.95 amplitude scaling factor. See Fig. 12 and ([18], pg. 179, Figs. 5.17, 5.18). This is consistent with our observations for f_z and f_y. See Fig. 12.

In the range observed, the amplitude effect is not that great, so that a best fit line can be used for the amplitude. Note the phase varies only slightly with piezo drive amplitude. A controller should be able to handle the slight nonlinearity in amplitude response and the phase delay. From these results, it appears the linear proportional model of the piezotube is reasonable within the frequency and amplitude range of interest.

7 Conclusion

The goal of this research is to develop a dynamic model to describe the large amplitude vibrations of a resonating fiber scanner. The difficulty in modeling is complicated by the fact that the effects of damping and nonlinearities are most influential in the resonant region. The partial integro-differential equations describing the continuum mechanics of a base excited cantilever were simplified leading to a set of ordinary state-space differential

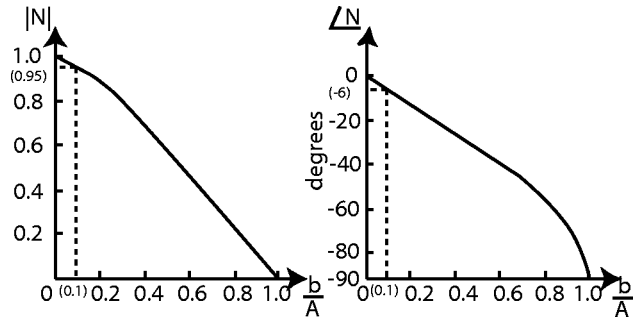

Fig. 12 Amplitude and phase angle of describing function N for backlash of width 2b and input amplitude A. ([18], pg. 179, figures 5.17, 5.18).

equations—the cross-coupled Duffing equations with centripetal acceleration. Damping models are included for the effects of internal damping and aerodynamic drag. A proportional model for the piezotube actuator is justified despite the known presence of nonlinearities such as hysteresis and creep.

Frequency responses were determined for the three types of actuation expected for the fiber scanner—raster scan, spiral scan, and propeller scan—using the Poincare-Lindstedt method. The responses exhibit an amplitude dependent phase, nonlinear amplitude response and the jump behavior for all three scan patterns. Using perturbation analysis, the response was shown to exhibit a cross-plane instability—whirl. Thus, the dynamic model is able to describe the main sources of scan distortion. The analytic frequency responses were compared with the experimentally measured frequency responses. Using the same parameters, the state-space dynamic model was shown to adequately predict the response of the vibrating fiber over the frequency range near resonance, over the amplitude range of operation, and for the three scan patterns.

The nonlinear spring behavior for the fiber's second mode vibration was shown to be softening for the raster scan, but hardening in the spiral scan. This difference in behavior is due to centripetal acceleration. The centripetal acceleration parameter and the nonlinear spring parameter cannot be determined individually from experimental frequency response curves of a single scan type, but the two parameters can be combined into a single equivalent nonlinear spring coefficient for each scan pattern. Using the equivalent nonlinear spring coefficients for the raster scan and the spiral scan, the two parameters can be determined. It also shown the effects of internal damping are dominant over the aerodynamic drag. Finally, the proportional model of the piezotube appeared appropriate and justified, thus removing the need for additional equations to handle the piezo dynamics.

The results of experiments show that an adequate model of the fiber scanner, including the actuator, fiber dynamics, and sensor can be given by

$$\ddot{p}+b\dot{p}+\omega_z^2 p=-\varepsilon p(p^2+q^2)+Cv_z \tag{37a}$$

$$\ddot{q}+b\dot{q}+\omega_y^2 q=-\varepsilon q(p^2+q^2)+Cv_y \tag{37b}$$

where the non-normalized natural frequencies are used, aerodynamic drag has been incorporated into the viscous damping term, an equivalent nonlinear spring coefficient appropriate for the scan pattern produced is used, and the piezotube amplitude nonlinearity is ignored.

A slightly more complex model would include aerodynamic drag and centripetal acceleration.

$$\ddot{p}+b\dot{p}+\alpha\dot{p}|\dot{p}|+\omega_z^2 p=-\varepsilon p(q^2+p^2)-\varepsilon_2 p(\dot{p}^2+\dot{q}^2)+Cv_z \tag{38a}$$

$$\ddot{q}+b\dot{q}+\alpha\dot{q}|\dot{q}|+\omega_y^2 q=-\varepsilon q(p^2+q^2)-\varepsilon_2 q(\dot{p}^2+\dot{q}^2)+Cv_y \tag{38b}$$

Since we desire a model which only keeps the essential dynamics in the operating range of interest, the first set of equations-the cross coupled Duffing with viscous damping (Eqs. 37*a*,*b*)-is recommended for the nonlinear controller. In this case, the nonlinear term can be computed using only position measurements. However, inclusion of the centripetal acceleration terms (Eqs. 38*a*,*b*) would most likely result in a better controlled transient response because these equations are for general excitation and do not assume a particular scan pattern. The use of the centripetal acceleration and/or aerodynamic drag terms would require additional velocity measurements, which are often not available and must be estimated.

Based on the nonlinear system model derived here (37*a*,*b*), several PID, linear, and nonlinear tracking controllers have been derived and simulated [2]. It was found that PID controllers can become unstable and linear controllers have steady state errors. Nonlinear robust state-space tracking controllers with feedback linearization were able to force the fiber to asymptotically track a reference.

Acknowledgment

This work has been sponsored by the Whitaker Foundation.

References

[1] Seibel, E. J., Smithwick, Q. Y. J., Brown, C. M., and Reinhall, P. G., 2001, ''Single Fiber Flexible Endoscope: General Design for Small Size, High Resolution, and Wide Field of View.'' *Biomonitoring and Endoscopy Technologies, Proceedings of the SPIE*; **4159**, pp. 29–39.

[2] Smithwick, Q. Y. J., Seibel, E. J., Reinhall, and P. G., Vagners, J., 2001, ''Control Aspects of the Scanning Single Fiber Flexible Endoscope.'' *Optical Fibers and Sensors for Medical Applications, Proceedings of the SPIE,* **4253,** pp. 176–188.

[3] Pai, P., and Nayfeh, A. H., 1990, ''Non-linear Non-planar Oscillations of a Cantilever Beam under Lateral Base Excitations,'' Int. J. Non-Linear Mech., **25**(5), pp. 455–474.

[4] Oueini, S. S., Nayfeh, A. H., 1999, ''Single-Mode Control of a Cantilever Beam Under Principal Parametric Excitation,'' J. Sound Vib., **224**(1), pp. 33–47.

[5] Haight, E. C., King, and W. W., 1972, ''Stability of Nonlinear Oscillations of an Elastic Rod,'' J. Acoust. Soc. Am., **52**(3-Part 2), pp. 899–911.

[6] Crespo da Silva, M. R. M., and Glynn, C. C., 1978, ''Nonlinear Flexural-Flexural Torsional Dynamics of Inextensional Beams I & II,'' J. Struct. Mech., **6**(4), pp. 437–461.

[7] Yang, Y. T., Heh, D., Wei, P. K., Fann, W. S., Gray, M. H., and Hsu, J. W. P., 15 Feb 1997, ''Vibration Dynamics of Tapered Optical Fiber Probes,'' J. Appl. Phys., **81**(4), pp. 1623–1627.

[8] Antognozzi, M., Binger, D. R., Humphris, A. D. L., James, P. J., and Miles, M. J., 2001, ''Modeling of cylindrically tapered cantilevers for transverse dynamic force microscopy (TDFM),'' Ultramicroscopy, **86**, pp. 223–232.

[9] Meirovitch, L., 1997, *Principles and Techniques of Vibrations*, Prentice Hall, pg. 120.

[10] Inman, D., 1994, *Engineering Vibration*, Prentice Hall.

[11] Thomson, W., 1988, *Theory of Vibration with Applications*, Prentice Hall, pg. 71.

[12] Chen, C. J., 1992, ''Electromechanical Deflections of Piezotubes with Quartered Electrodes,'' Appl. Phys. Lett., **60**, pg. 132.

[13] Croft, D., and Devasia, S., 1997, ''High Precision Positioning Stages for micro/nano Lithography,'' *International Society for Optical Engr., Proceedings of the SPIE*, **3225**, pp. 68–75.

[14] Ho, C. H., Scott, R. A., and Eisley, J. G., 1975, ''Non-Planar, Non-Linear Oscillations of a Beam—I. Forced Motions,'' Int. J. Non-Linear Mech., **10**(2), pp. 113–127.

[15] Jordan, D. W., 1979, *Nonlinear Ordinary Differential Equations*, Oxford University Press, pg. 129.

[16] Seibel, E. J., Smithwick, Q. Y. J., Crossman-Bosworth, J., and Myers, J. A., 2002, ''Prototype Scanning Fiber Endoscope,'' *Optical Fibers and Sensors for Medical Applications II, Proceedings of the SPIE*, **4616**, pp. 173–179.

[17] Nayfeh, A. H., 2000, *Nonlinear Interactions: Analytic, Computational, and Experimental Methods*, Wiley-Interscience Publication.

[18] Slotine, J. J., Li, W. L., 1992, Applied Nonlinear Control, New Jersey: Prentice-Hall.